Large Stress-Gradient Creep Tests and Model Establishment for Red Sandstone Treated at High Temperatures

Xiaopeng Ren [1,2,3], **Yajun Xin** [4,5,*], **Baoshan Jia** [1], **Kun Gao** [1], **Xuping Li** [2] **and Yu Wang** [4]

1   Institute of Mining, Liaoning Technical University, Fuxin 123000, China
2   College of Mining and Coal, Inner Mongolia University of Science and Technology, Baotou 014010, China
3   Beijing Tiandi Huatai Mining Management Co., Ltd., Beijing 100003, China
4   School of Energy Science and Engineering, Henan Polytechnic University, Jiaozuo 454000, China
5   Collaborative Innovation Center of Coal Work Safety and Clean High Efficiency Utilization, Jiaozuo 454000, China
*   Correspondence: xinyj@hpu.edu.cn; Tel.: +86-135-6912-0613

Abstract: Red sandstone samples treated at high temperatures feature complex creep properties. Uniaxial compression tests and the incremental creep tests at different stress gradients were conducted on 10 red sandstone samples of the same specifications divided into five groups on an RLW-2000 triaxial servo rheometer in the laboratory. Relationships of the instantaneous strain and creep strain of red sandstone samples treated at high temperatures with the stress level were explored, and the creep properties and strength of the samples at different temperature gradients were investigated. In addition, the creep failure patterns and failure mechanism of the red sandstone samples were determined, and a creep constitutive model was established for the samples considering the effects of temperature. The conformity between test data and theoretical curves was discussed. Results show that as the stress increases, the instantaneous strain tends to decrease rapidly, slowly, then increase slowly; the creep strain tends to decrease, steadily increase, then increase substantially. At the same stress, as the stress gradient is doubled, the instantaneous strain decreases by 47.45%, and the creep strain decreases by 48.30%. For samples treated at 300~900 °C, the number of stress levels experienced gradually decreases; as the temperature increases, the creep failure strength of samples first increases, then decreases in an arcuate form, and the creep strain tends to decrease, increase, then increase rapidly. In the temperature range, the creep strain at the two stress gradients has a growing difference, with the maximum difference reaching 0.0134%; there is an inflection point at 300 °C in the creep failure strength of samples. At the same stress, the more the stress levels experienced, the lower the creep failure strength, and the temperature, creep failure strength, and creep strain can be characterized by a quadratic polynomial. At 300 °C, mineral particles in samples are sintered and cemented into chains, and there is a significant primary control plane, so the samples show oblique shear failure of a single primary control plane. At 600~900 °C, particles and blocks in samples begin to be sintered and flow, and the cemented chains are broken. Under the condition, the samples mainly show failure dominated by mixed and crossed primary and secondary control planes and crushing failure due to transverse compression. The established Burgers–Kelvin-Temperature (BKT) creep constitutive model is sensitive to changes in temperature; the theoretical curves are consistent with the test data.

Keywords: red sandstone; high-temperature creep; gradient damage; strength characteristic; creep property; failure mode; constitutive model

1. Introduction

Many steeply dipping coal seams occur in western China. Due to the large dip angle, these coal seams are often on fire at the outcrop. After burning, many high-quality coal

resources remain in the burned area. To develop these coal resources, studying the long-term stability of surrounding rocks of the burned areas is of critical significance for safe mining of coal resources.

In recent years, some progress has been achieved in relevant research on the damage mechanism [1–3] and mechanical properties [4,5] of rock after high-temperature treatment. Sheng-Qi et al. analyzed the temperature influence on the deformation behaviors of the red sandstone specimens and proposed the concept of the temperature–strain rate to describe the relationship between strain and temperature [6,7]. Zhang et al. studied the micro-damage mechanisms and the macroscopic responses to the progressive process of thermal damage of sandstone by measuring the macroscopic physical-mechanical properties and the microscopic properties of red sandstone heated at various temperatures up to 800 °C [8]. Xu et al. established a formula for the triaxial compressive strength of coarse-grained sandstone containing the temperature and strength threshold of surrounding rock [9]. Chen et al. formulated a creep model to describe the time-dependent deformation of granite at different temperatures [10]. Xu et al. propose here a two-dimensional, thermo-mechanical numerical model to describe the time-dependent brittle creep of low-porosity granite under different constant temperatures and confining pressures [11]. Su et al. evaluated correlations of the mineral compositions, structural characteristics, and mechanical parameters of fine sandstone treated at high temperatures with the temperature from a microscopic perspective [12]. Xu et al. found that the temperature influences the failure mode of granite under uniaxial compression [13]. Qin et al. studied the relationships of changes in the thermal expansion stress with the lithology, disintegration of internal minerals, and changes in the speed of sound in the rock [14].

In order to investigate the influence of temperature, confining pressure, and preexisting fissure on creep characteristics of rock mass, Wang et al. performed multistage creep experiments on shale-like material, with preexisting fissure under different temperatures and confining pressures [15]. Ye et al. found more influence of temperature on the peak strength and creep failure time than on the residual strength and volume change [16]. Pan et al. found the high temperature reduced the ability of the red sandstone to resist instantaneous deformation and creep deformation [17]. In terms of high-temperature creep and constitutive model, Xin et al. studied the basic creep properties and strength characteristics of red sandstone [18]. Hu et al. analyzed the relationships of the time-related deformation and creep loading, the instantaneous modulus, and the permeability on sandstones considering thermally induced damage [19]. Yang et al. studied creep characteristics of pre-cracked sandstone specimens with permeability measurement [20]. Sha et al. studied the changes in tensile strength and brittleness of sandstones and granites with temperature and corresponding mechanisms [21]. Sharma et al. investigated the elastic, strength, and creep properties of organic-rich shales by a combination of nano indentation, energy dispersive X-ray spectroscopy, and micromechanical modeling over a range of temperatures (23–350 °C) [22]. Shibata et al. analyzed creep behavior of the soft rocks of impermeable nature under high temperature [23]. Li et al. revealed the underlying mechanism of thermal-induced deformation and cracking of salt at grain scale and investigated the micro-mechanisms of how temperature influences salt creep behavior [24,25]. Zhang et al. established the thermal damage variable based on the Weibull distribution and continuum damage mechanics theory for studying the temperature effect on creep deformation of deep coal [26]. Chen et al. investigated the influence of temperature and stress condition on the creep properties of Beishan granite [27]. Liu et al. investigated physical and mechanical properties of granite and sandstone samples after high-temperature treatment and explored the differences in temperature effects on the physical and mechanical characteristics [28].

Some damage model on temperature for rocks were studied recently. Zhang et al. established a damage model for rocks under freeze-thaw and loading effects based on residual strength characteristics [29]. Song et al. studied the creep properties of red sandstone in a low-temperature environment and established a model thereof [30]. Zhang et al. found that the creep stress threshold of gneissic granite decreases with increasing tempera-

ture [31]. To study the creep constitutive model of rocks after high-temperature treatment, Zhou et al. built a creep constitutive model for gas and coal under triaxial stress at high temperatures [32]. Wang et al. established a constitutive model for the whole creep process of granite at different temperatures, which elucidates the influences of key parameters including the elastic modulus and viscosity coefficient on key creep parameters of granite [33]. Considering two influencing factors, namely, temperature and volumetric strain, Xue et al. established a fractional-order Burgers creep damage model [34]. Based on the temperature-stress coupling, Zhou et al. established a time-dependent damage model of rocks [35]. Xi et al. constructed a rheological model for granite under thermo-dynamic coupling [36]. Shan et al. built a three-dimensional creep model for frozen bedded red sandstone based on the freeze-thaw conditions [37].

The aforementioned research mainly focuses on basic mechanical properties and establishment of relevant creep models of rocks at high temperatures. These studies provide a basis for exploring incremental creep properties of high-temperature red sandstone. By using an RLW-2000 triaxial servo-motor-controlled rheometer, uniaxial compression and incremental creep tests at different stress gradients were conducted on 10 red sandstone samples of the same specifications divided into five groups. In this way, the relationships between the instantaneous strain and creep strain with the stress on red sandstone samples treated at high temperatures were studied and the creep properties and strength of the samples at different temperature gradients were expounded. In addition, the creep failure patterns and failure mechanism of red sandstone samples were determined, and a creep constitutive model of red sandstone samples considering the temperature effect was established. The research results provide reference for the control theory and technology for the long-term stability of surrounding rocks of roadways in the burned areas at the outcrop of coal seams.

2. Materials and Test Methods

2.1. Sample Preparation

(1) Sample sources: hard red sandstone of uniform particle sizes was used in the tests. It was bronzing in the natural state, containing a few visible textures. With an average density of 2.103 g/cm^3, the rock mainly contained minerals including quartz, feldspar, and illite.

(2) Sample preparation: a core-drilling machine and a cutting machine were used to machine the red sandstone blocks into standard samples (cylinders measuring Φ 50 $\times$ L 100 mm). Then, a grinding machine was used to grind the samples until the unevenness of the two end faces was less than 0.05 mm.

(3) Sample grouping: the homogeneity of prepared samples was tested, and samples with high homogeneity and consistent textures were divided into five groups (A to E) and labelled A1, A2, B1, B2, . . . , with two samples in each group. The grouping and labelling of samples are shown in Figure 1.

Figure 1. Group number of red sandstone specimens.

(4) Preparation of high-temperature samples. A SX2-5-12 intelligent box-type muffle furnace was used to treat six samples in groups C, D, and E at high temperatures (300, 600, and 900 °C) (Figure 2).

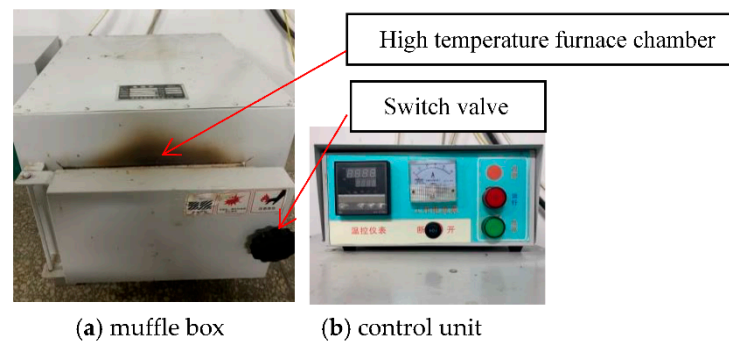(**a**) muffle box   (**b**) control unit

Figure 2. SX2-5-12 Smart box muffle furnace.

Samples in each group were heated from the room temperature (25 °C) to the pre-set temperatures (with the temperature difference controlled to within ±10 °C) at a rate of 10 °C/min. After allowing the samples to stand at a constant temperature for 30 min, the furnace was opened and the samples removed. Basic characteristics of the samples treated at high temperatures are listed in Table 1.

Table 1. The basic characteristics of red sandstone specimens.

Group	No.	Diameter/mm	Height/mm	Weight/g	Density/g/cm^3	Height–Diameter Ratio
Uniaxial compression	A1	49.72	99.34	405.79	2.10	2.00
	A2	49.62	98.86	404.94	2.12	1.99
Creep (25 °C)	B1	49.62	99.42	425.06	2.21	2.00
	B2	49.72	100.20	411.89	2.12	2.02
Creep (300 °C)	C1	49.74	99.70	401.88	2.07	2.00
	C2	49.62	98.84	400.76	2.10	1.99
Creep (600 °C)	D1	49.92	99.32	424.02	2.18	1.99
	D2	49.94	92.90	375.63	2.06	1.86
Creep (900 °C)	E1	50.06	100.26	402.76	2.04	2.00
	E2	50.02	99.86	398.17	2.03	2.00

2.2. Test Methods

The creep tests were conducted on the RLW-2000 triaxial rheometer for rocks (Figure 3). The displacement-controlled loading mode was used in the tests, and the applied stress and displacement changes of samples in the process were automatically collected using the test software.

Figure 3. RLW-2000 rock triaxial rheology servo rheometer.

(1) Uniaxial compression scheme.

Uniaxial compression tests were conducted on samples in group A (A1 and A2) at a loading rate of 0.05 mm/s, to determine basic mechanical parameters and provide a basis for determining the initial stress level and stress gradients in the creep tests.

(2) Determination of initial stress.

The initial stress in the creep tests was determined to be 60% of the average uniaxial compressive strength of samples in group A.

(3) Creep test schemes

The creep tests of different stress increments and gradients were conducted on eight samples in groups B to E. Incremental creep tests were performed on samples 1 and 2 in each group at stresses of 2.5 and 5 MPa, respectively.

The specific test design is described as follows: the upper end face of labelled samples was brought into contact with the axial compression end of the triaxial rheometer and the dial indicator of displacement was zeroed. Displacement-controlled loading (0.05 mm/s) was adopted to apply load to the first stress; after 24 h of creep, the loading continued at a rate of 0.05 mm/s to the pre-set second stress; after 24 h of creep, the stress was increased to the third level. Incremental creep tests at each stress were conducted at stress gradients separately of 2.5 and 5.0 MPa for samples 1 and 2 in each group, followed by 24 h of creep (to failure of samples). The loading paths used in these tests are shown in Figure 4, and the specific characteristics of samples in the tests are summarized in Table 2.
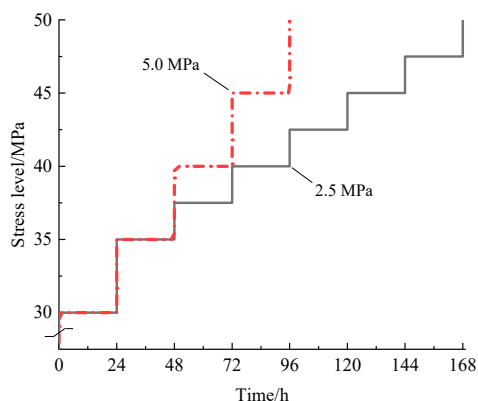

Figure 4. Test loading ways.

Table 2. The test characteristics of red sandstone specimens.

Temperature/°C	Group	Loading Rate/mm/s	Test Way				
			Uniaxial Compression	Incremental Load Creep			
			No.	Initial Stress/MPa	Creep Time/h	Gradient Level/MPa	
25	A	0.05	A1/A2	/	/	2.5 (Group 1)	5.0 (Group 2)
	B					B1	B2
300	C	0.05	/	30	24	C1	C2
600	D					D1	D2
900	E					E1	E2

3. Results and Discussion

The stress–strain curves of samples A1 and A2 under uniaxial compression are demonstrated in Figure 5, and those of groups B to E in the creep tests are shown in Figure 6. The creep test results are listed in Table 3.
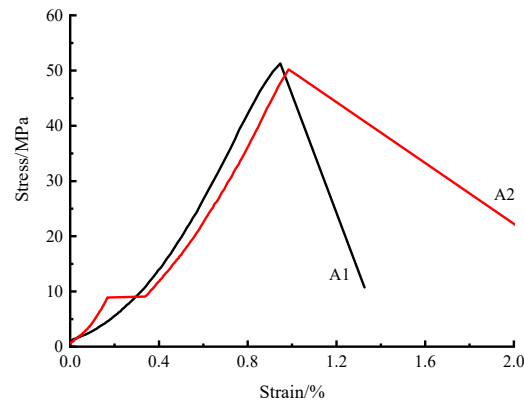
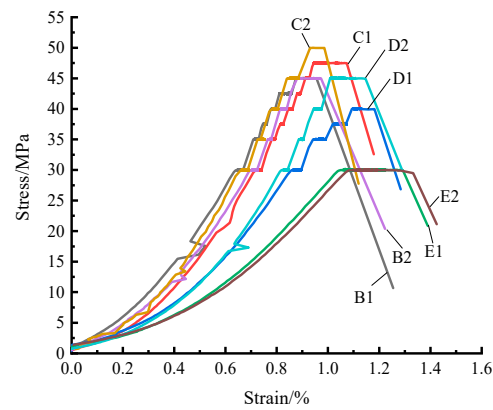**Figure 5.** Stress–strain curves on uniaxial compression.

Figure 6. Stress–strain curves on incremental load creep.

The peak strengths of samples A1 and A2 under uniaxial compression are separately 51.66 and 50.21 MPa, with an average uniaxial compressive strength of 50.93 MPa. Fractures develop in local areas of sample A2 in the uniaxial compression process, while the sample still has a peak strength similar to that of sample A1, so initial fracture of the sample exerts slight influences on the mechanical properties. The initial stress level in creep tests was set to be about 60% of the uniaxial compression strength, that is, 30 MPa. Curves in the creep tests are illustrated in Figure 7.
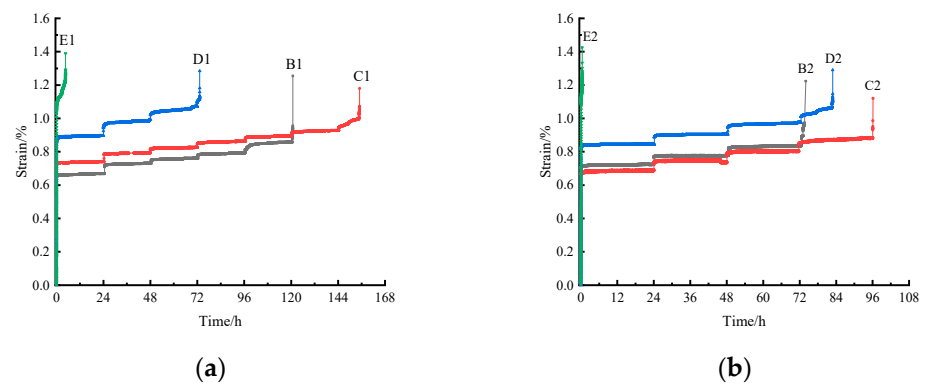

(**a**)

(**b**)

Figure 7. Creep curves of red sandstone specimens. (**a**) Gradient level in 2.5 MPa. (**b**) Gradient level in 5.0 MPa.

Table 3. The data of creep test.

Group	No.	Stress/MPa	Load/kN	Strain before Creep/%	Strain after Creep/%	Instantaneous Strain%	Creep Strain/%	Creep Time/h	Creep Failure Strength/MPa
Creep (25 °C)	B1	30	58.01	0.6437	0.6689	0.6437	0.0251	24.6006	45
		35	67.68	0.7121	0.7302	0.0433	0.0181	23.8029	
		37.5	72.52	0.7463	0.7614	0.0161	0.0151	23.9566	
		40	77.35	0.7785	0.7936	0.0171	0.0151	24.1217	
		42.5	82.18	0.8097	0.8580	0.0161	0.0483	24.0806	
		45	87.02	0.8821	0.9555	0.0241	0.0734	0.2809	
	B2	30	58.25	0.7066	0.7236	0.7066	0.0170	24.0259	45
		35	67.95	0.7675	0.7784	0.0439	0.0110	24.5313	
		40	77.66	0.8124	0.8373	0.0339	0.0250	24.0273	
		45	87.37	0.8802	0.9731	0.0429	0.0928	1.0157	
Creep (300 °C)	C1	30	58.01	0.7234	0.7406	0.7234	0.0172	24.3455	47.5
		35	67.68	0.7811	0.7932	0.0405	0.0121	23.6529	
		37.5	72.52	0.8134	0.8256	0.0202	0.0121	24.0547	
		40	77.35	0.8458	0.8620	0.0202	0.0162	24.5314	
		42.5	82.18	0.8812	0.8934	0.0192	0.0121	23.7301	
		45	87.02	0.9126	0.9268	0.0192	0.0142	24.0281	
		47.5	91.85	0.9439	1.0735	0.0172	0.1296	10.6067	
	C2	30	58.29	0.6630	0.6871	0.6630	0.0241	24.0191	50
		35	68.01	0.7252	0.7362	0.0381	0.0110	24.0208	
		40	77.73	0.7813	0.8034	0.0451	0.0221	23.6617	
		45	87.44	0.8405	0.8826	0.0371	0.0421	24.3511	
		50	97.16	0.9308	0.9859	0.0481	0.0551	0.0306	
Creep (600 °C)	D1	30	58.76	0.8633	0.8956	0.8633	0.0323	24.0521	40
		35	68.56	0.9408	0.9914	0.0452	0.0506	24.0364	
		37.5	73.45	1.0194	1.0721	0.0280	0.0527	23.9193	
		40	78.35	1.0936	1.1819	0.0215	0.0883	1.2440	
	D2	30	58.72	0.8226	0.8447	0.8226	0.0222	24.1718	45
		35	68.5	0.8860	0.9041	0.0413	0.0181	24.1737	
		40	78.29	0.9464	0.9746	0.0423	0.0282	24.0783	
		45	88.07	1.0089	1.1106	0.0342	0.1017	10.4171	
Creep (900 °C)	E1	30	59.05	1.0513	1.2926	1.0513	0.2413	4.6029	30
	E2	30	58.95	1.0925	1.2848	1.0925	0.1923	0.3394	30

3.1. Relationships of the Stress with the Instantaneous Strain and Creep Strain

Relationships between the stress and the instantaneous strain are shown in Figure 8. Because the initial stress level of samples is 30 MPa, which is 58.90% of the uniaxial compressive strength and six and twelve times the stress in normal test design, the initial instantaneous strain is large. The instantaneous strain is about 0.6437% to 1.0925%, which is 0.8208% on average. During loading to the first stress, internal fractures (voids) are mainly compacted in the samples.

After reaching the second stress level (35 MPa) (samples E1 and E2 are not analyzed because they were damaged at the first stress), the average instantaneous strain in samples B1 to D1 is 0.0430% while that in B2 to D2 is 0.0411% when the stresses on samples 1 and 2 are both increased by 5.0 MPa. Therefore, the average instantaneous strain at a stress of 35 MPa is 0.0421%, which decreases significantly (by 94.87%) compared with that at the first stress level and is manifest as the constant compaction of samples.
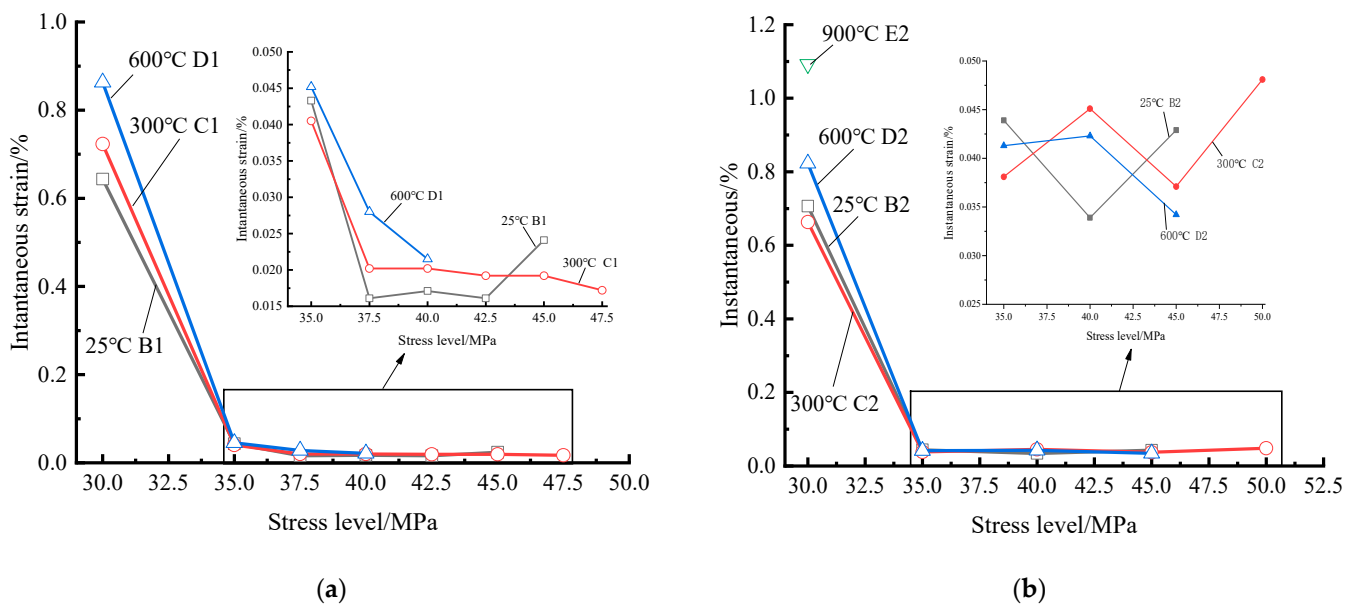
Figure 8. The relationship of instantaneous strain and stress level. (**a**) Gradient level in 2.5 MPa. (**b**) Gradient level in 5.0 MPa.

After reaching the third stress level, the stress gradient differs for samples 1 and 2 in each group. The average instantaneous strain in samples B1 to D1 (at a stress of 37.5 MPa) is 0.0241%, while that in B2 to D2 (40.0 MPa) is 0.0411%, which shows that the instantaneous strain differs slightly at the same stress gradients, with a difference of 0.0170%. The stress gradient is correlated with the instantaneous strain. At the third stress level, plastic fractures and slight particle rotation develop within the samples.

At the same stresses (40 and 45 MPa separately for samples 1 and 2) corresponding to different stress gradients, the average instantaneous strains in B1 to D1 are 0.0196% and 0.0217% (0.0207% on average), and those in B2 to D2 are 0.0404% and 0.0381% (0.0391% on average), respectively. Fractures (voids) in the samples are coalesced and particles are rotated to a greater extent. In the final stage, the instantaneous strain increases compared with the previous level, signaling the advent of failure.

The instantaneous strain on samples tends to undergo an abrupt decrease at first, then a slow decrease, and finally a slow increase with increasing stress. At the same stresses (40 and 45 MPa separately for samples 1 and 2 samples), the average instantaneous strain in sample 1 in each group (stress gradient of 2.5 MPa) is 0.0206%, which is 47.45% lower than the average value of 0.0393% found in sample 2 (stress gradient of 5.0 MPa). The instantaneous strain has multiple relationships with the stress gradient: samples treated at 300 °C can sustain a larger number of stress levels, while for samples treated at 600 to 900 °C, the number of stress levels decreases successively. The lower the number of stress levels, the larger the instantaneous strain.

The relationships between the stress level and creep strain are displayed in Figure 9; because the first stress applied is 30 MPa, with a large relative gradient, the creep strain is large. In addition, creep failure occurs to samples in group E, causing the initial creep strain to increase, so that the average creep strain reaches 0.0714% and voids in the samples enter the compaction stage. Then, as the stress increases to 35 MPa for all samples, the average creep strain is 0.0202%, decreasing by 71.71%. At a stress of 40 MPa, the average creep strain reaches 0.0325%, which is 60.89% higher than that at a stress of 35 MPa. When the stress rises to 45 MPa, the creep strain is increased by 88.62% from 0.0325% to 0.0613%. At a stress of 50 MPa (not considering sample 1 in each group), the increase in creep strain slows.
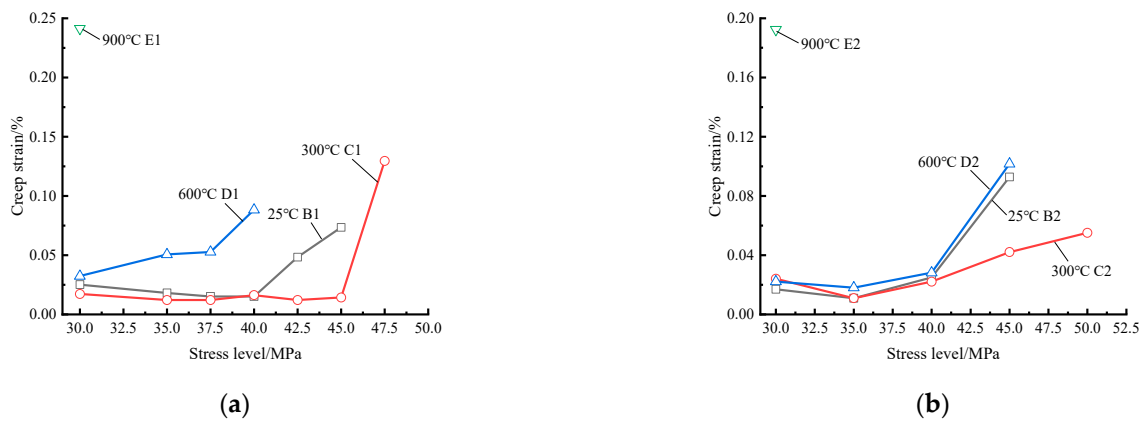
Figure 9. The relationship of creep strain and stress level. (**a**) Gradient level in 2.5 MPa. (**b**) Gradient level in 5.0 MPa.

The creep of samples 1 and 2 in each group shows an increasing trend at the stress gradient of 5.0 MPa and the change is between 60.89% and 88.62%. Creep intensifies damage to the samples. The creep strain at the last level is aggravated, indicating the advent of the final failure of the samples.

The creep strain in samples tends to decrease, increase steadily, then substantially with increasing stress. At different temperature gradients, the creep strain in samples treated at 300 °C is less than that at room temperature; at 600~900 °C, the creep strain exceeds that at room temperature at the same stress gradient. At a stress (40 MPa, without final creep failure) corresponding to different stress gradients, the average creep strain of sample 1 in each group (stress gradient of 2.5 MPa) at 40 MPa is 0.0152%, which is 48.30% lower than that sample 2 (stress gradient of 5.0 MPa) (0.0294%). The result indicates that the number of stress levels significantly influences the creep strain.

3.2. Relationships of Temperature with Creep Failure Strength and Creep Strain

After high-temperature treatment, the relationships between the temperature and the creep failure strength of samples are shown as curves in Figure 10. At the room temperature (25 °C), the average creep failure strength is 45 MPa; then, as the temperature rises to 300 °C, the creep failure strengths of samples 1 and 2 are separately 47.5 and 50 MPa, with an average of 48.75 MPa, which is 8.33% higher than that at 25 °C. Particles in the samples flow, are sintered, and linked; crystals such as SiO_2 are molten and cemented, thus increasing the creep failure strength of samples.
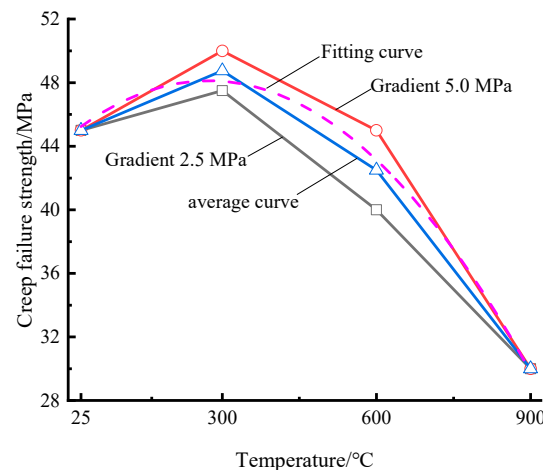

Figure 10. The relationship of creep failure strength and temperature.

As the temperature increases to 600 and 900 °C, the average creep failure strengths are separately 42.5 and 30 MPa, which are 5.56% and 33.33% lower than that at room temperature (25 °C), respectively. From 300 to 600 °C, the average creep failure strength decreases by 12.82% from 48.75 to 42.5 MPa; from 600 to 900 °C, it is decreased by 29.41% from 42.5 to 30 MPa. This indicates that the decrease of the creep failure strength increases, which means that rising temperature exerts significant influences on the strength of such samples.

By fitting the relationship between the temperature and the creep failure strength of samples, we find that

$$\sigma_c = 44.6279 + 0.0255T - 4.6687 \times 10^{-5}T^2 \tag{1}$$

where σ_c and T separately represent the creep failure strength and the treatment temperature of samples, $R^2 = 0.9852$.

The fitting equation characterizes the relationship between the temperature and the creep failure strength.

The creep failure strength of samples first increases and then decreases to show an arcuate shape with increasing temperature, with an inflection point at 300 °C. The more stress levels are sustained, the lower the creep failure strength at the same stress, that is, the number of stress levels significantly influences the strength of such samples.

The relationship between the temperature and creep strain of samples after high-temperature treatment is shown in Figure 11.
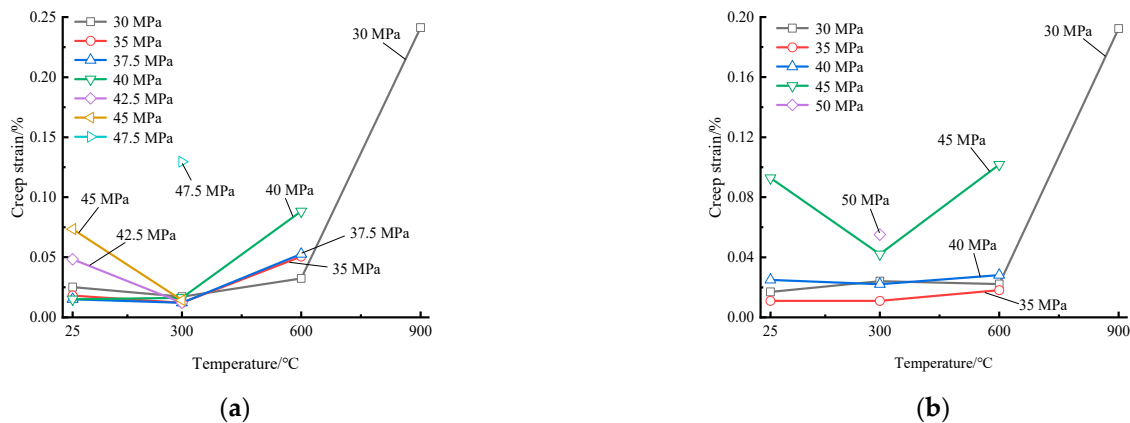

Figure 11. The relationship of creep strain and temperature. (**a**) Gradient level in 2.5 MPa. (**b**) Gradient level in 5.0 MPa.

At room temperature (25 °C), the creep strain in sample 1 in each group (stress gradient of 2.5 MPa) is in the range of 0.0151%~0.0251%, while that of sample 2 (stress gradient of 5.0 MPa) changes between 0.0110% and 0.0250% at stresses of 30~40 MPa, both changing slightly. At stresses of 42.5~45 MPa, the creep strains in samples 1 and 2 in each group (stress gradients of 2.5 and 5.0 MPa, respectively) are 0.0483%~0.0734% and 0.0928%, with large changes therein. When treated at 300 °C, grains are recrystallized and fine particles are molten and sintered in samples, so the strength of samples increases and therefore influences of the stress level on creep strain decreases. At 600 °C, the greater the stress, the greater the creep strain; at 900 °C, the creep strain is maximized, reaching 0.2168% on average because the samples are damaged at the first stress level.

The values of creep strain at different temperatures are averaged (Figure 12) and the creep data are displayed in Table 4.
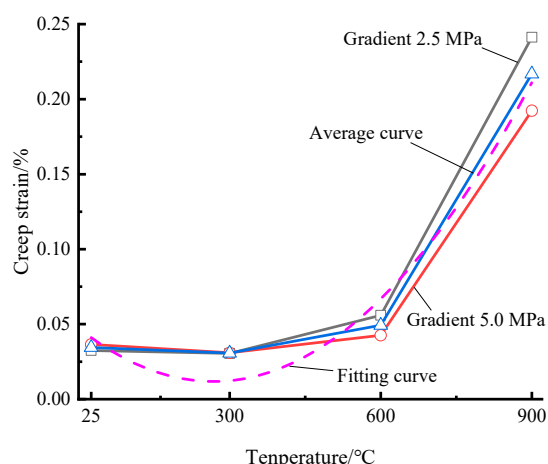
Figure 12. The relationship of creep strain average and temperature.

Table 4. The relationship of creep strain and temperature.

Temperature/°C		25	300	600	900
Creep strain/%	Group 1	0.0325	0.0305	0.0560	0.2413
	Group 2	0.0365	0.0309	0.0426	0.1923
	Mean value of sum	0.0345	0.0307	0.0493	0.2168
	Differences	−0.0040	−0.0004	0.0134	0.0490

At room temperature (25 °C), the average values of creep strain of samples at stress gradients of 2.5 and 5.0 MPa are 0.0325% and 0.0365%, respectively, with a difference of −0.004 and an average of 0.0345%. After increasing the temperature to 300 °C, the strength of the samples increases and the average creep strains at stress gradients of 2.5 and 5.0 MPa are 0.0140% and 0.0248%, respectively. At that temperature, the difference decreases to −0.0004, and the average is 0.0307%, which is 11.01% lower than that at the room temperature (25 °C), indicative of an improvement in the stability of such samples.

As the temperature is increased to 600 °C, the average creep strains at stress gradients of 2.5 and 5.0 MPa are 0.0560% and 0.0426%. Their difference begins to increase to 0.0134%, and their average is 0.0493, which is 60.59% higher than that at 300 °C. The increase in creep strain reduces the stability of the samples. As the temperature rises to 900 °C, samples E1 and E2 both experience creep failure after application of one stress level, and their creep strain is 0.2413% and 0.1923%, respectively. The difference in creep strain abruptly increases to 0.0490%, and the average is 0.2168%, which grows by 339.77% compared with that at 600 °C, accompanied by accelerated failure of samples.

The creep strain in all samples and the difference in creep strains in samples 1 and 2 in each group both change in a similar manner (decreasing at first, then increasing steadily, then rapidly), as the temperature is increased. At 600 °C, the difference in creep strain at the two stress gradients grows, with the maximum of 0.0134% (the case at 900 °C is not considered because the stress gradients are not different at that temperature). The result indicates that the temperature and stress gradient significantly influence the creep strain.

The relationship between the temperature and creep strain of samples is fitted; then,

$$\varepsilon_c = 0.0474 - 2.6634 \times 10^{-4}T + 4.9793 \times 10^{-7}T^2 \tag{2}$$

where ε_c represents the creep strain, $R^2 = 0.9700$.

The correlation coefficients are lower than those between the temperature and creep failure strength, while the fitting equation can still be used to reveal the relationship between the temperature and creep strain.

3.3. Creep Failure Patterns

The creep failure patterns of samples at different temperature gradients after tests are shown in Figure 13 (A1 and A2 are failure patterns after uniaxial compression of samples). The failure patterns of eight red sandstone samples in the creep tests are illustrated in Figure 14.
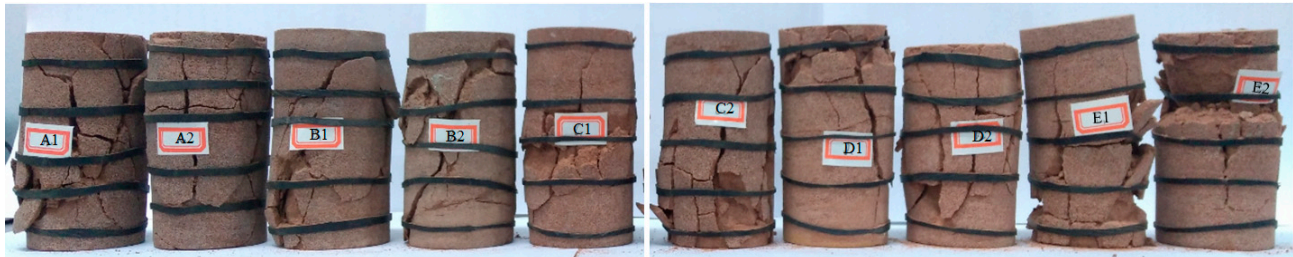

Figure 13. Creep failure morphology of red sandstone specimens.
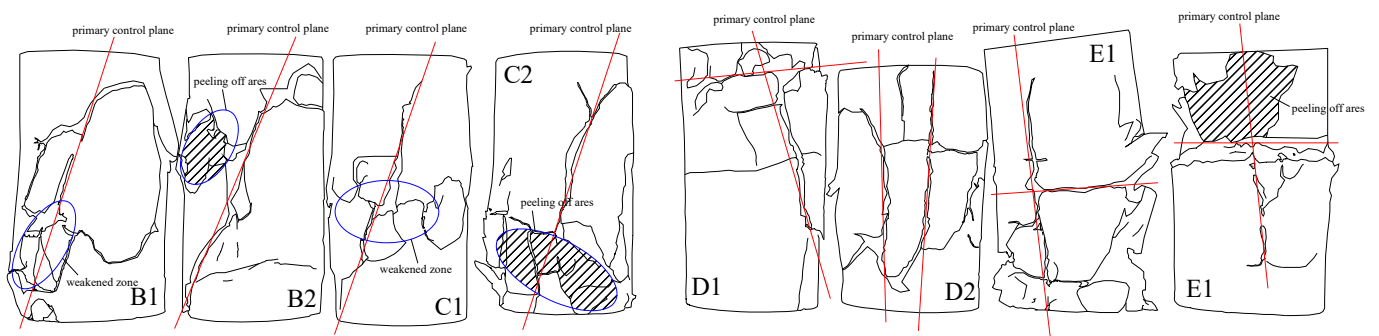

Figure 14. The sketch on creep failure specimens.

Figures 13 and 14 indicate that the failure patterns of samples are closely correlated with the temperature: for failure patterns of samples at 25 °C (B1 and B2), oblique shear failure with a single primary control plane is observed, and the plane differs in the direction with large blocks spalling in local areas. At 300 °C, samples are stronger, and the primary shear fracture planes have smaller width and depth than those in samples at 25 °C. In addition, there are obvious oblique primary control planes, significant shear failure characteristics, lower strength weakening, and a certain lumpiness of the samples. For samples tested at 600 °C (D1 and D2) and 900 °C (E1 and E2), more primary control planes appear with the rising temperature gradient due to sintering at high temperatures, changes in mineral composition, and opening of internal free fractures. As a result, the failure patterns, which are shown as shear-tensile mixed fracture planes and appearance of transverse fracture vertical to the loading direction of samples, become more complex.

The strength of samples treated at 300 °C increased, so the primary control plane is significant in the failure pattern, with significant lumpiness. As the temperature is increased above 300 °C, the strength of samples gradually decreases, characteristics of primary control planes become less obvious, the lumpiness decreases, and shear characteristics gradually disappear. For samples in the same group, the lower the stress gradient, the more numerous the fractures and the more complex the failure patterns of such samples.

In order to further explore the microscopic structural characteristics of samples after being treated at different temperatures, samples treated at 25, 300, 600, and 900 °C were studied by observations at a magnification of ×1000 (Figure 15).

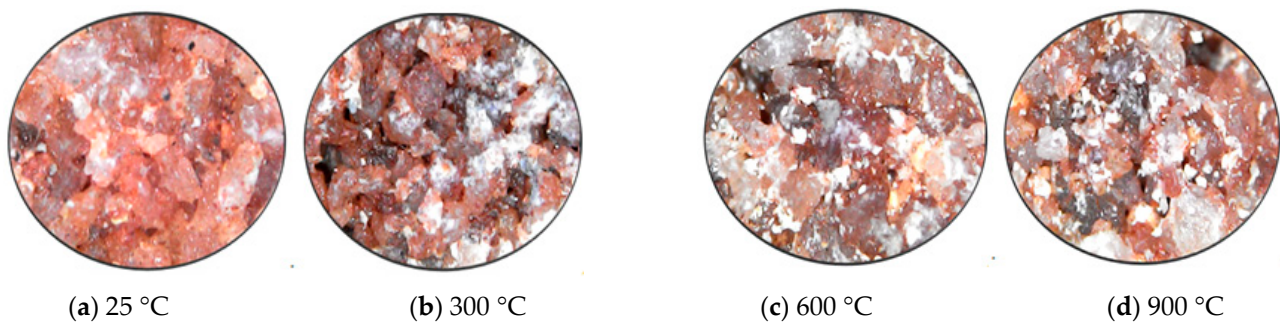| (a) 25 °C | (b) 300 °C | (c) 600 °C | (d) 900 °C |

Figure 15. The meso-morphology of specimen structure.

The sample surface is reddish, particles are relatively uniform and regular, and structures in the samples are loose at room temperature (25 °C). As the samples are heated to 300 °C, the surface is darkened, and particles are molten and sintered to form new minerals that are a result of the connection of large particles. Due to sintering and flow of particles, voids between particles enlarge while cemented chains of particles are compact. These are the main cause for the improved strength of samples at 300 °C. When the samples are heated to 600 °C, the surface becomes slightly lighter in colored; large, sintered blocks begin to be damaged and flow; particles become smaller; structures are loosened, and some cemented chains are broken, so that the plastic flow is enhanced, and the strength of samples decreases. When the temperature increases further to 900 °C, recrystallization is observed on the sample surface; transgranular fractures appear; there are significant thermal fractures, and structures are extremely loose. In addition, the sample color changes to pale red, indicative of changes in mineral composition, which intensify the reductions in the strength.

4. Failure Mechanism and Constitutive Model

4.1. Creep Failure Mode and Mechanism

The temperature remarkably influences the strength of samples by separately increasing and decreasing the strength. After being heated to 300 °C, the samples are strengthened, and damaged samples are lumpy, with an obvious single primary control plane. The failure of samples is mainly shown as sudden shear failure along the diagonal. For samples heated to and above 600 °C, their strength is decreased, and the damaged samples have a lower lumpiness, with less obvious primary control planes and appearance of secondary control planes, contributing to complex failure patterns. When the temperature rises to 900 °C, internal structures are disordered, and cemented chains are broken in the samples; failure is mainly shown as crushing failure due to transverse compression. Therefore, the failure modes of high-temperature red sandstone samples include oblique shear failure with a single primary control plane, failure dominated by mixed and crossed primary and secondary control planes and crashing failure due to transverse compression.

In the creep process of samples, the incremental creep of samples always shows the three-stage characteristic of conventional creep tests, and different temperature gradients change the strain energy needed for creep failure of samples. After being heated to 300 °C, the thermo-dynamic coupling sinters minerals and cements voids, thus increasing the strain energy needed for creep failure, as evinced by the increased strength of samples. At temperatures above 300 °C, high-strength compositions in the samples, such as SiO_2, begin to be molten and disintegrated, and the cemented chains are broken. The high temperature causes internal damage to samples, which significantly decreases the strain energy needed for creep failure, making failure more likely.

4.2. Elements with Creep Damage Considering the Temperature Effect

The tests indicate that the temperature significantly influences the strength, instantaneous strain, and creep strain in red sandstone samples. Therefore, the elastic modulus

E and viscosity η of the rocks also change with the temperature, manifest in the forms $E = E(T)$ and $\eta = \eta(T)$. Due to influences of the stress gradients (accumulation of damage), the damage variable *D* is introduced to characterize changes in the elastic modulus.

The temperature effect and damage accumulation in the creep process are combined to establish elements with creep damage considering the temperature effect, as shown in Figure 16.
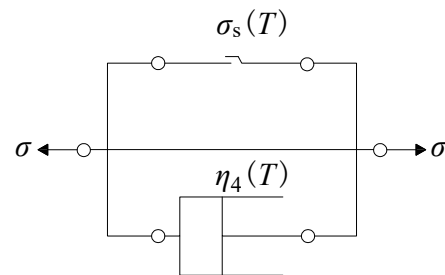

Figure 16. Creep damage elements on temperature effect.

According to the damage mechanics, the damage variable is defined as

$$D(T,\sigma,t) = 1 - \frac{E(T,\sigma,t)}{E_0(T)} \tag{3}$$

where $E_0(T)$ represents the initial elastic modulus at temperature *T*; $E(T,\sigma,t)$ denotes the elastic modulus at temperature *T* and stress level σ at any time.

According to existing research findings [38], $E(T,\sigma,t)$ is defined as

$$E(T,\sigma,t) = E_0(T) \cdot e^{-\alpha(T)t} \tag{4}$$

where $\alpha(T)$ represents the material coefficient of samples at temperature *T*.

Substituting Equation (4) into Equation (3):

$$D(T,\sigma,t) = 1 - e^{-\alpha(T)t} \tag{5}$$

According to definition of the effective stress in the damage mechanics:

$$\widetilde{\sigma}(T) = \frac{\sigma}{1 - D(T,\sigma,t)} \tag{6}$$

where $\widetilde{\sigma}(T)$ and σ denote the effective stress and the Cauchy stress, both at temperature *T*, respectively.

Substituting Equation (5) into Equation (6):

$$\widetilde{\sigma}(T) = \sigma \cdot e^{\alpha(T)t} \tag{7}$$

For those elements with creep damage considering the temperature effect, the strain rate is expressed as follows:

$$\dot{\varepsilon}_{\mathrm{III}}(T) = \frac{\widetilde{\sigma}(\mathrm{T}) - \sigma_s(T)}{\eta_4(T)} = \frac{\sigma \cdot e^{\alpha(T)t} - \sigma_s(T)}{\eta_4(T)} \tag{8}$$

where $\dot{\varepsilon}_{\mathrm{III}}(T)$ is the strain rate of elements with creep damage considering the temperature effect at temperature *T*; $\sigma_s(T)$ represents the long-term strength at temperature *T*; $\eta_4(T)$ denotes the viscosity coefficient of elements with creep damage considering the temperature effect at temperature *T*.

Through integral operation on Equation (6) under the initial condition $t = 0$ and $\varepsilon_{III}(T) = 0$, the constitutive equation of elements with creep damage considering the temperature effect is obtained:

$$\varepsilon_{III}(T) = \frac{\sigma}{\alpha(T)\eta_4(T)}\left[e^{\alpha(T)t} - 1\right] - \frac{\sigma_s(T)}{\eta_4(T)}t \tag{9}$$

The creep curves of samples related to α are plotted (Figure 17a) by setting element parameter $\alpha(T)$ to be 0.10, 0.08, 0.06, and 0.04, and substituting the viscosity coefficient of samples $\eta_4 = 5 \times 10^7$ MPa·h at $\sigma = 40$ MPa, $\sigma_s = 30$ MPa, and temperature T in Equation (9). Similarly, creep curves of samples related to η_4 are obtained (Figure 17b) by setting η_4 to 5×10^4, 5×10^6, 5×10^8, and 5×10^{10} and substituting $\alpha(T) = 0.1$ for samples under $\sigma = 40$ MPa, $\sigma_s = 30$ MPa, and temperature T to Equation (9).

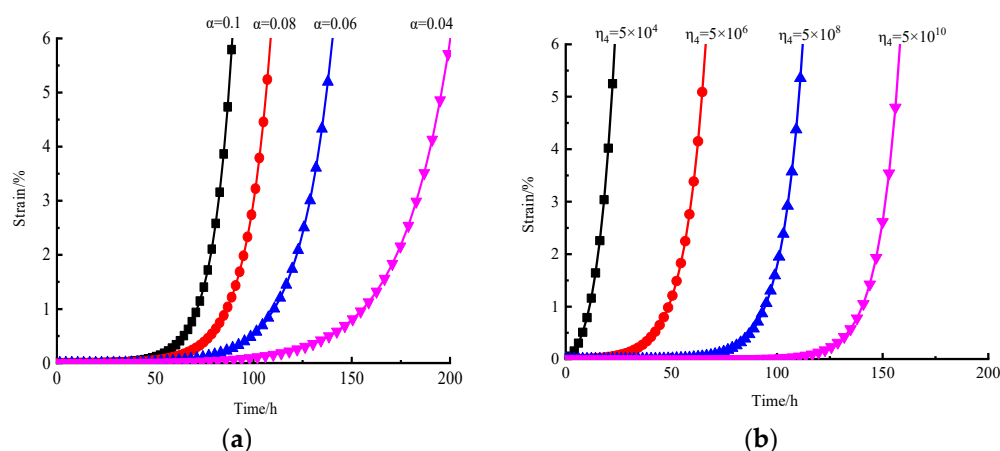**Figure 17.** The creep curves of damage elements on temperature effect. (**a**) $\alpha(T)$ Sensitivity. (**b**) η_4 Sensitivity.

The time when the samples enter the accelerated creep stage delays with the reduction of α, and the larger the value of α is, the steeper the creep curves and the more substantially the creep changes per unit time. The greater the viscosity, the later the samples enter the accelerated creep stage. The damage element considering the temperature effect can characterize the accelerated creep process in such samples.

4.3. High-Temperature Creep Constitutive Model

Considering the significant influences of the stress level, stress gradient, and temperatures on the strength and creep strain of samples during loading, the Kelvin model and the basic elements with creep damage considering the temperature effect are connected in series in the Burgers model. In this way, a new Burgers–Kelvin-temperature (B-K-T) high-temperature creep constitutive model was established (Figure 18).
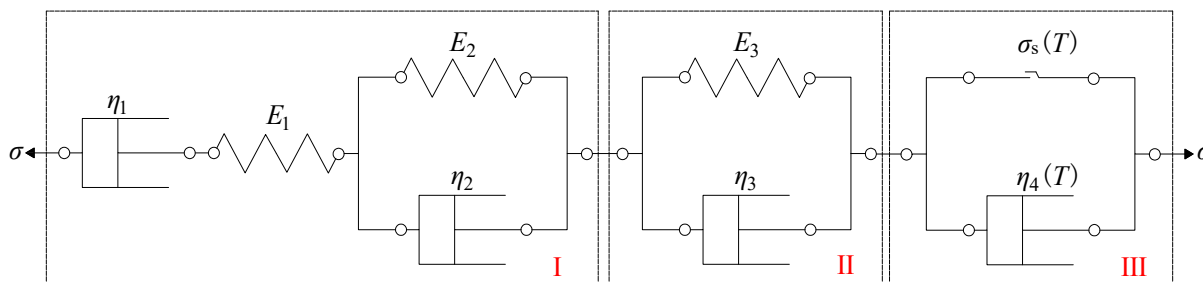

Figure 18. Creep constitutive model of red sandstone specimens subjected to high temperature.

According to the basic principle for connecting elements in series, the total stress of the combination is identical to the stress of any element connected in series, and the total strain equals the sum of the strains (I, II, and III) of all elements connected in series. It is supposed that the total stress is σ, then the total strain is expressed as:

$$\varepsilon = \varepsilon_{\mathrm{I}} + \varepsilon_{\mathrm{II}} + \varepsilon_{\mathrm{III}} \tag{10}$$

The creep constitutive model of Burgers bodies is

$$\varepsilon_{\mathrm{I}} = \frac{\sigma}{\eta_1} t + \frac{\sigma}{E_1} + \frac{\sigma}{E_2}\left(1 - e^{-\frac{E_2}{\eta_2} t}\right) \tag{11}$$

The creep constitutive model of Kelvin bodies is

$$\varepsilon_{\mathrm{II}} = \frac{\sigma}{E_3}\left(1 - e^{-\frac{E_3}{\eta_3} t}\right) \tag{12}$$

For elements with creep damage considering the temperature effect,

$$\varepsilon_{\mathrm{III}} = \begin{cases} 0, \sigma \le \sigma_s \\ \frac{\sigma}{\alpha(T)\eta_4(T)}\left[e^{\alpha(T)t} - 1\right] - \frac{\sigma_s(T)}{\eta_4(T)} t, \sigma > \sigma_s \end{cases} \tag{13}$$

In summary, the creep constitutive equation for the high-temperature creep model of red sandstone can be expressed as follows:

(1) When $\sigma \le \sigma_s$, the creep damage model considering the temperature effect fails, so the creep constitutive equation is

$$\varepsilon = \sigma\left[\frac{1}{\eta_1} t + \frac{1}{E_1} + \frac{1}{E_2}\left(1 - e^{-\frac{E_2}{\eta_2} t}\right) + \frac{1}{E_3}\left(1 - e^{-\frac{E_3}{\eta_3} t}\right)\right] \tag{14}$$

(2) When $\sigma > \sigma_s$, the creep damage model considering the temperature effect is effective, so the creep constitutive equation is

$$\varepsilon = \sigma\left[\frac{1}{\eta_1} t + \frac{1}{E_1} + \frac{1}{E_2}\left(1 - e^{-\frac{E_2}{\eta_2} t}\right) + \frac{1}{E_3}\left(1 - e^{-\frac{E_3}{\eta_3} t}\right)\right] + \frac{\sigma}{\alpha(T)\eta_4(T)}\left[e^{\alpha(T)t} - 1\right] - \frac{\sigma_s(T)}{\eta_4(T)} t \tag{15}$$

4.4. Verification of the High-Temperature Creep Model

To judge whether the high-temperature creep model of red sandstone is accurate and reasonable or not, the Levenberg–Marquardt method and global optimization method are used for parametric inversion of test data. Here, taking the test results of samples at two stress levels (30 MPa, $\sigma \le \sigma_s$ and 40 MPa, $\sigma > \sigma_s$) and different temperature gradients (25, 300, and 600 °C) and the high-temperature creep constitutive model considering the temperature effect as examples, regression analysis is performed on E_1, E_2, E_3, η_1, η_2, η_3, η_4, and α according to test data, to obtain the theoretical curves. The fitting results are displayed in Table 5, and the comparison results of the test data and theoretical curves are illustrated in Figure 19.

Table 5. The results of parameter fitting.

| Stress Level/MPa	Temperature/°C	E_1/GPa	E_2/GPa	E_3/GPa	η_1/10^3 GPa·h^{-1}	η_2/MPa·h^{-1}	η_3/GPa·h^{-1}	η_4/GPa·h^{-1}	α
	25	4.32×10^6	313.202	4.246	8.320	3.89×10^4	0.085		
30	300	1.93×10^8	4.516	203.792	6.874	98.552	27.272		
	600	7.28×10^4	3.592	488.488	26.822	120.028	813.594		
	25	1.43×10^5	4.881	483.040	11.653	4.192	529.763	3.09×10^7	0.371
40	300	12.903	8.446	235.748	46.848	6.921	194.849	2.16×10^8	0.418
	600	4.96	525.640	3.591	27.553	1.01×10^6	0.044	3.99×10^{11}	0.826
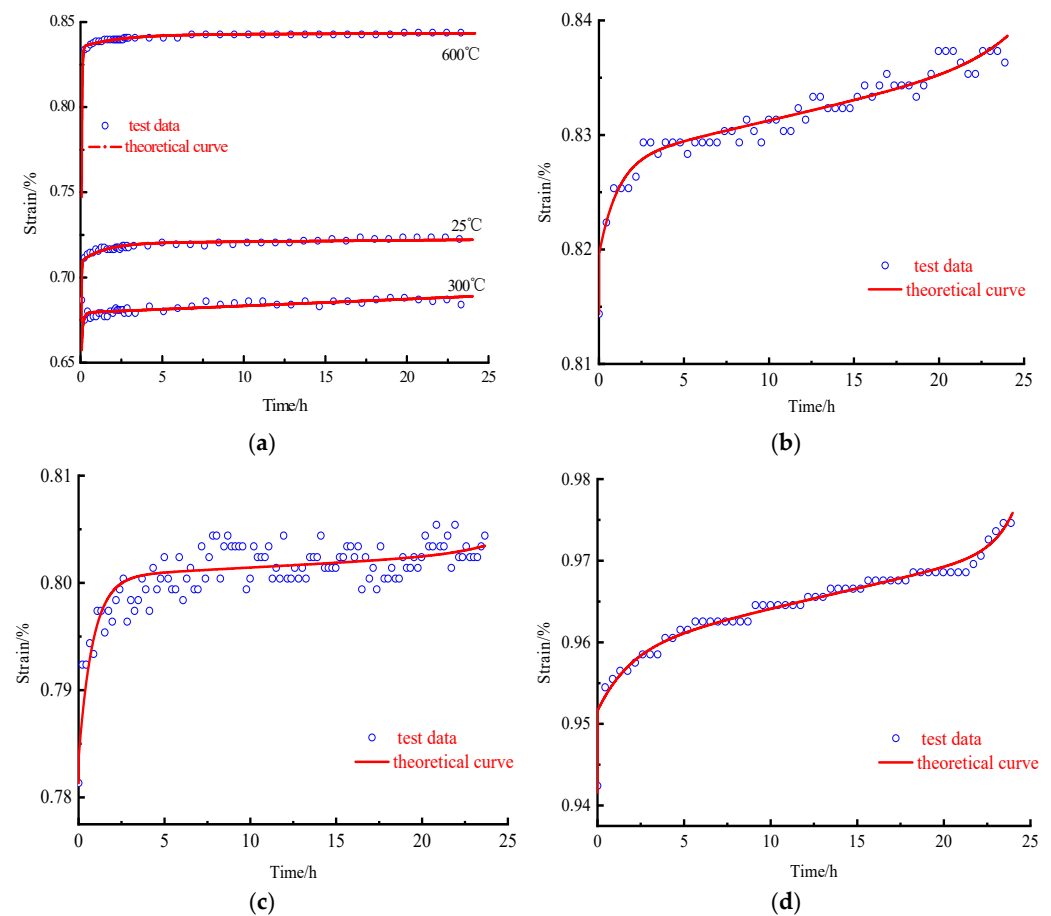
Figure 19. The comparison between test data and theoretical curves. (**a**) σ = 30 MPa (B2, C2, D2). (**b**) T = 25 °C, σ = 40 MPa (B2). (**c**) T = 300 °C, σ = 40 MPa (C2). (**d**) T = 600 °C, σ = 40 MPa (D2).

The comparison of theoretical curves and test data shows that the theoretical curves of samples at 25, 300, and 600 °C have correlation coefficients R^2 of 0.79, 0.79, and 0.70 (0.76 on average) with the test data at a low stress level (30 MPa, $\sigma \leq \sigma_s$, failure of elements with creep damage considering the temperature effect); while at a high stress level (40 MPa, $\sigma > \sigma_s$, elements with creep damage considering the temperature effect being effective), the correlation coefficients R^2 of theoretical curves of samples at 25, 300, and 600 °C with the test data are 0.94, 0.70, and 0.98, with an average of 0.87. The result indicates that the theoretical curves obtained using the B-K-T high-temperature creep constitutive model considering the temperature effect match the test data well. Therefore, establishing the B-K-T high-temperature creep constitutive model considering the temperature effect for red sandstone can represent the influence of temperature on the creep damage in red sandstone samples under high stresses.

5. Conclusions

To explore complex creep properties of red sandstone subjected to high temperature, the incremental creep tests at different stress gradients on five groups of red sandstone samples and its theoretical analysis were conducted. The conclusions are as follows.

(1) As the stress increases, the instantaneous strain of samples changes in a trend of first abrupt decrease, then slow decrease, and slow increase. At the same stress, the instantaneous strain is decreased by 47.45% if the stress gradient is doubled. For samples treated at 300 to 900 °C, the number of stress levels experienced by samples decreases successively. The larger the number of stress levels, the lower the instantaneous strain.

(2) With the increase in the stress, the creep strain of samples tends to decrease, increase steadily, then do so substantially. At the same stress, the creep strain decreases by 48.30%

when the stress gradient is doubled. The creep strain in samples heated to 300 °C is smaller, while that in samples treated at 600 and 900 °C is larger, than that at room temperature (25 °C).

(3) As the temperature rises, the creep failure strength of samples first increases and then decreases in arcuate form, with an inflection point at 300 °C. At the same stress, the larger the number of stress levels sustained, the lower the creep failure strength. The relationship between the temperature and the creep failure strength is characterized by a quadratic polynomial.

(4) As the temperature is increased, the creep strain in such samples first decreases, then increases steadily, and then increases rapidly: the difference in creep strain at the two stress gradients increases with the maximum difference reaching 0.0134%. The quadratic polynomial relationship used to characterize the temperature and the creep strain becomes less significant.

(5) Mineral particles in samples heated to 300 °C are sintered and cemented, with a significant primary control plane therein, so the samples show oblique shear failure with a single primary control plane. Particles and blocks in samples treated at 600 and 900 °C begin to be sintered and flow, and the cemented chains are slowly broken. Under the condition, samples mainly show failure dominated by mixed and crossed primary and secondary control planes and crashing failure due to transverse compression.

(6) The B-K-T creep constitutive model considering the temperature effect was established and parameters in the model were subjected to inversion analysis. The model is sensitive to changes in temperature, and its theoretical curves match the test data to an acceptable extent.

Author Contributions: Conceptualization, X.R.; formal analysis and investigation, Y.X.; writing—review and editing, B.J.; methodology, K.G.; writing—original draft preparation, X.L.; data curation, Y.W. All authors have read and agreed to the published version of the manuscript.

Conflicts of Interest: The authors declare no conflict of interest.

References

1. Zhu, Z.N.; Jiang, G.S.; Tian, H.; Wu, W.B.; Liang, R.Z.; Dou, B. Study on statistical thermal damage constitutive model of rock based on normal distribution. *J. Cent. South Univ.* **2019**, *50*, 1411–1418. (In Chinese)
2. Wang, M.N.; Hu, Y.P.; Tong, J.J.; Wang, Q.L.; Wang, Y.C.; Dong, C.Y. Experimental study on shear mechanical properties and thermal damage model of shotcrete-rock interfaces under variable high temperatures. *Chin. J. Rock Mech. Eng.* **2019**, *38*, 63–75. (In Chinese)
3. Zhao, Y.Y.; Wei, K.; Zhou, J.Q.; Li, X.; Chen, Y.F. Laboratory study and micromechanical analysis of mechanical behaviors of three thermally damaged rocks. *Chin. J. Rock Mech. Eng.* **2017**, *36*, 142–151. (In Chinese)
4. Li, J.G.; Wang, Y.Y. Experimental analysis of temperature effect in creep of soft rock. *J. China Coal Soc.* **2012**, *37*, 81–85. (In Chinese)
5. Hou, D.; Peng, J. Triaxial mechanical behavior and strength model for thermally-damaged marble. *Chin. J. Rock Mech. Eng.* **2019**, *38*, 2603–2613. (In Chinese)
6. Yang, S.Q.; Hu, B.; Ranjith, P.G.; Xu, P. Multi-step loading creep behavior of red sandstone after thermal treatments and a creep damage model. *Energies* **2018**, *11*, 212. [CrossRef]
7. Yang, S.Q.; Hu, B. Creep and long-term permeability of a red sandstone subjected to cyclic loading after thermal treatments. *Rock Mech. Rock Eng.* **2018**, *51*, 2981–3004. [CrossRef]
8. Zhang, W.Q.; Sun, Q.; Zhu, Y.M.; Guo, W.H. Experimental study on response characteristics of micro–macroscopic performance of red sandstone after high-temperature treatment. *J. Therm. Anal. Calorim.* **2019**, *136*, 1935–1945. [CrossRef]
9. Xu, C.B.; Zhou, H.S. Test investigation of triaxial compressive strength of coarse sandstone after high temperature. *Chin. J. Rock Mech. Eng.* **2016**, *35*, 2811–2818. (In Chinese)

10. Chen, L.; Wang, C.P.; Liu, J.F.; Liu, Y.M.; Liu, J.; Su, R.; Wang, J. A damage-mechanism-based creep model considering temperature effect in granite. *Mech. Res. Commun.* **2014**, *56*, 76–82. [CrossRef]

11. Xu, T.; Zhou, G.L.; Heap, M.J.; Zhu, W.C.; Chen, C.F.; Baud, P. The influence of temperature on time-dependent deformation and failure in granite: A mesoscale modeling approach. *Rock Mech. Rock Eng.* **2017**, *50*, 2345–2364. [CrossRef]

12. Su, C.D.; Wei, S.J.; Yang, Y.S.; Qin, B.D. Analysis of strength and conventional triaxial compression deformation characters of coarse sandstone after high temperature. *Chin. J. Rock Mech. Eng.* **2015**, *34*, 2792–2800. (In Chinese)

13. Xu, X.L.; Gao, F.; Zhang, Z.Z.; Chen, L. Experimental study of the effect of loading rates on mechanical properties of granite at real-time high temperature. *Rock Soil Mech.* **2015**, *36*, 2184–2192. (In Chinese)

14. Qin, B.D.; Luo, Y.J.; Men, Y.M.; Chen, L.J. Experimental research on swelling properties of limestone and sandstone at high temperature. *Rock Soil Mech.* **2011**, *32*, 417–422+473. (In Chinese)

15. Wang, Y.Y.; Wang, H.W.; Shi, X. Creep investigation on shale-like material with preexisting fissure under coupling temperatures and confining pressures. *Adv. Civ. Eng.* **2019**, *9*, 7861305. [CrossRef]

16. Ye, G.L.; Nishimura, T.; Zhang, F. Experimental study on shear and creep behaviour of green tuff at high temperatures. *Int. J. Rock Mech. Min. Sci.* **2015**, *79*, 19–28. [CrossRef]

17. Pan, X.K.; Berto, F.; Zhou, X.P. Creep damage behaviors of red sandstone subjected to uniaxial compression after high-temperature heat treatment using acoustic emission technology. *Fatigue Fract. Eng. Mater. Struct.* **2022**, *45*, 302–322. [CrossRef]

18. Xin, Y.J.; An, D.C.; Li, M.Y.; Hao, H.C. Creep and strength characteristics of post-peak stage loading in high strength red-sandstone. *J. China Coal Soc.* **2017**, *42*, 1714–1723. (In Chinese)

19. Hu, B.; Yang, S.Q.; Tian, W.L. Creep-permeability behavior of sandstone considering thermal-damage. *Geomech. Eng.* **2019**, *18*, 71–83. [CrossRef]

20. Yang, S.Q.; Tang, J.Z.; Elsworth, D. Creep rupture and permeability evolution in high temperature heat-treated sandstone containing pre-existing twin flaws. *Energies* **2021**, *14*, 6362. [CrossRef]

21. Sha, S.; Rong, G.; Tan, J.; He, R.H.; Li, B.W. Tensile strength and brittleness of sandstone and granite after high-temperature treatment: A review. *Arab. J. Geosci.* **2020**, *13*, 598. [CrossRef]

22. Sharma, P.; Prakash, R.; Abedi, S. Effect of temperature on nano- and microscale creep properties of organic-rich shales. *J. Pet. Sci. Eng.* **2019**, *175*, 375–388. [CrossRef]

23. Shibata, K.; Tani, K.; Okada, T. Creep behavior of tuffaceous rock at high temperature observed in unconfined compression test. *Soils Found.* **2007**, *47*, 1–10. [CrossRef]

24. Li, W.J.; Zhu, C.; Yang, C.H.; Duan, K.; Hu, W.R. Experimental and DEM investigations of temperature effect on pure and interbedded rock salt. *J. Nat. Gas Sci. Eng.* **2018**, *56*, 29–41. [CrossRef]

25. Li, W.J.; Han, Y.H.; Wang, T.; Ma, J.W. DEM micromechanical modeling and laboratory experiment on creep behavior of salt rock. *J. Nat. Gas Sci. Eng.* **2017**, *46*, 38–46. [CrossRef]

26. Zhang, L.; Zhou, H.W.; Wang, X.Y.; Wang, L.; Su, T.; Wei, Q.; Deng, T.F. A triaxial creep model for deep coal considering temperature effect based on fractional derivative. *Acta Geotech.* **2022**, *17*, 1739–1751. [CrossRef]

27. Chen, L.; Liu, J.F.; Wang, C.P.; Liu, J.; Wang, J. Experimental investigation on the creep behaviour of beishan granite under different temperature and stress conditions. *Eur. J. Environ. Civ. Eng.* **2015**, *19*, s43–s53. [CrossRef]

28. Liu, S.; Xu, J.Y. An experimental study on the physico-mechanical properties of two post-high-temperature rocks. *Eng. Geol.* **2015**, *185*, 63–70. [CrossRef]

29. Zhang, H.M.; Meng, X.Z.; Peng, C.; Yang, G.S.; Ye, W.J.; Shen, Y.J.; Liu, H. Rock damage constitutive model based on residual intensity characteristics under freeze-thaw and load. *J. China Coal Soc.* **2019**, *44*, 3404–3411. (In Chinese)

30. Song, Y.J.; Zhang, L.T.; Ren, J.X.; Chen, J.X.; Che, Y.X.; Yang, H.M.; Bi, R. Creep property and model of red sandstone under low temperature environment. *J. China Coal Soc.* **2020**, *45*, 2795–2803. (In Chinese)

31. Zhang, Q.Y.; Zhang, L.Y.; Xiang, W.; Jiang, L.Y.; Ding, Y.Z. Triaxial creep test of gneissic granite considering thermal effect. *Rock Soil Mech.* **2017**, *38*, 2507–2514. (In Chinese)

32. Zhou, C.B.; Wan, Z.J.; Zhang, Y.; Liu, Y.; Zhang, B. Creep characteristics and constitutive model of gas coal mass under high temperature and triaxial stress. *J. China Coal Soc.* **2012**, *37*, 2020–2025. (In Chinese)

33. Wang, C.P.; Chen, L.; Liang, J.W.; Liu, J.; Liu, Y.M.; Liu, J.F.; Wang, J.; Zhou, H.W. Creep constitutive model for full creep process of granite considering thermal effect. *Rock Soil Mech.* **2014**, *35*, 2493–2500+2506. (In Chinese)

34. Xue, D.J.; Lu, L.L.; Yi, H.Y.; Wu, Z.D.; Zhang, Q.S.; Zhang, Z.P. A fractional Burgers model for uniaxial and triaxial creep of damaged salt-rock considering temperature and volume-stress. *Chin. J. Rock Mech. Eng.* **2021**, *40*, 315–329. (In Chinese)

35. Zhou, G.L.; Xu, T.; Zhu, W.C.; Chen, C.F.; Yang, T.H. A time-dependent thermo-mechanical creep model of rock. *Eng. Mech.* **2017**, *34*, 1–9+25. (In Chinese) [CrossRef]

36. Xi, B.P.; Zhao, Y.S.; Wan, Z.J.; Zhao, J.C.; Wang, Y. Study of constitutive equation of granite rheological model with thermo-mechanical coupling effects. *Chin. J. Rock Mech. Eng.* **2009**, *28*, 956–967. (In Chinese)

37. Shan, R.L.; Bai, Y.; Sun, P.F.; Sui, S.M.; Huang, Y.L.; Chen, J.L. Study of triaxial creep mechanical properties and constitutive model of frozen stratified red sandstone. *J. China Univ. Min. Technol.* **2019**, *48*, 12–22. (In Chinese)

38. Wu, G.; Zhai, S.T.; Wang, Y. Research on characteristics of mesostructure and acoustic emission of granite under high temperature. *Rock Soil Mech.* **2015**, *36*, 351–356. (In Chinese)